OATAO
Open Archive Toulouse Archive Ouverte

Open Archive Toulouse Archive Ouverte (OATAO)

OATAO is an open access repository that collects the work of Toulouse researchers and makes it freely available over the web where possible

This is an author's version published in: **http://oatao.univ-toulouse.fr/19354**

Ultra-high-rate pseudocapacitive energy storage in two-dimensional transition metal carbides

Maria R. Lukatskaya[1,2†‡], Sankalp Kota[2‡], Zifeng Lin[3,4‡], Meng-Qiang Zhao[1,2], Netanel Shpigel[5], Mikhael D. Levi[5], Joseph Halim[1,2], Pierre-Louis Taberna[3,4], Michel W. Barsoum[2], Patrice Simon[3,4]★ and Yury Gogotsi[1,2]★

The use of fast surface redox storage (pseudocapacitive) mechanisms can enable devices that store much more energy than electrical double-layer capacitors (EDLCs) and, unlike batteries, can do so quite rapidly. Yet, few pseudocapacitive transition metal oxides can provide a high power capability due to their low intrinsic electronic and ionic conductivity. Here we demonstrate that two-dimensional transition metal carbides (MXenes) can operate at rates exceeding those of conventional EDLCs, but still provide higher volumetric and areal capacitance than carbon, electrically conducting polymers or transition metal oxides. We applied two distinct designs for MXene electrode architectures with improved ion accessibility to redox-active sites. A macroporous $Ti_3C_2T_x$ MXene film delivered up to $210\,F\,g^{-1}$ at scan rates of $10\,V\,s^{-1}$, surpassing the best carbon supercapacitors known. In contrast, we show that MXene hydrogels are able to deliver volumetric capacitance of $\sim 1{,}500\,F\,cm^{-3}$ reaching the previously unmatched volumetric performance of RuO_2.

Typical commercial batteries require prolonged charging and therefore are limiting mobility of users. Systems that are capable of delivering high energy densities at relatively high charge/discharge rates are classified as pseudocapacitors and characterized by absence of phase transformations during operation[1–3]. Pseudocapacitors are a sub-class of supercapacitors that are differentiated from electrical double-layer capacitors (EDLCs) on the basis of charge storage mechanism. EDLCs store charge via formation of the electrical double layer at the electrode/electrolyte interface and, naturally, their capacitance is proportional to the electrode's specific surface area available for electrosorption of ions. Pseudocapacitors, on the other hand, utilize fast redox reactions and therefore can potentially provide higher energy densities due to charge transfer.

Since the discovery of high specific capacitances in RuO_2 (refs 4–7), research on other pseudocapacitive materials (for example, MnO_2 (ref. 8), MoO_3 (ref. 9), Nb_2O_5 (refs 10,11), VN (ref. 12)) has attracted much attention, but the limited electronic conductivity of most pseudocapacitive oxides leads to high electrode resistance and, consequently, lower power densities compared with EDLCs and electrolytic capacitors. Conductive coatings on electrochemically active materials[10] and hybrids of active materials and conductive phases[6,11] enhance charge transfer, but rapid transport of ions and electrons to all active sites remains a challenge, especially when the electrode thickness exceeds a few micrometres. Synthesis of materials with large, open channels (for example, T-Nb_2O_5 (ref. 12)) allowed rapid ion access and significantly improved rate capability over existing high-rate redox materials, such as $Li_4Ti_5O_{12}$, but the issue of low electronic conductivity remained. Therefore, pseudocapacitors usually operate at rates that are between those of batteries and double-layer capacitors[3].

MXenes are a class of two-dimensional materials[13], usually produced by selective etching of layered ternary transition metal carbides called MAX phases in acidic fluoride containing solutions, such as lithium fluoride (LiF) solution in hydrochloric acid (HCl)[14]. MXenes have a general formula $M_{n+1}X_nT_x$, where 'M' is a transition metal, X is C and/or N, n is an integer between 1 and 3, and T_x represent surface functional groups[13]. As depicted in Fig. 1a, MXenes' unique structure renders them particularly attractive for energy storage applications because: a conductive inner transition metal carbide layer enables fast electron supply to electrochemically active sites; a transition metal oxide-like surface generated during the synthesis[15] is redox active; a two-dimensional morphology and pre-intercalated water[14] enable fast ion transport. Previously, high volumetric capacitances of freestanding MXene electrodes of ~ 900 and $700\,F\,cm^{-3}$ were demonstrated for $Ti_3C_2T_x$ (ref. 14) and Mo_2CT_x (ref. 16), respectively, yet their charging at rates above $100\,mV\,s^{-1}$ remained largely unexplored. Herein, we probe the limits of pseudocapacitive charge storage in terms of rate, capacitance and voltage window using $Ti_3C_2T_x$ and Mo_2CT_x and demonstrate how effective electrode design strategies allow energy storage and delivery at ultrahigh rates. We demonstrate how highly accessible macroporous electrode architectures enable exceptional high-rate performance with capacitance over $200\,F\,g^{-1}$ at $10\,V\,s^{-1}$ rate. We also show using MXene hydrogel that *in situ* incorporation of the H_2SO_4 electrolyte in between MXene layers enables volumetric capacitance of $\sim 1{,}500\,F\,cm^{-3}$.

Theoretical capacitance and voltage window

Previously, we demonstrated that the mechanism of charge storage in $Ti_3C_2T_x$ in one molar sulfuric acid, $1\,M\,H_2SO_4$, is pseudocapacitive; that is, changes in electrode potential correlate
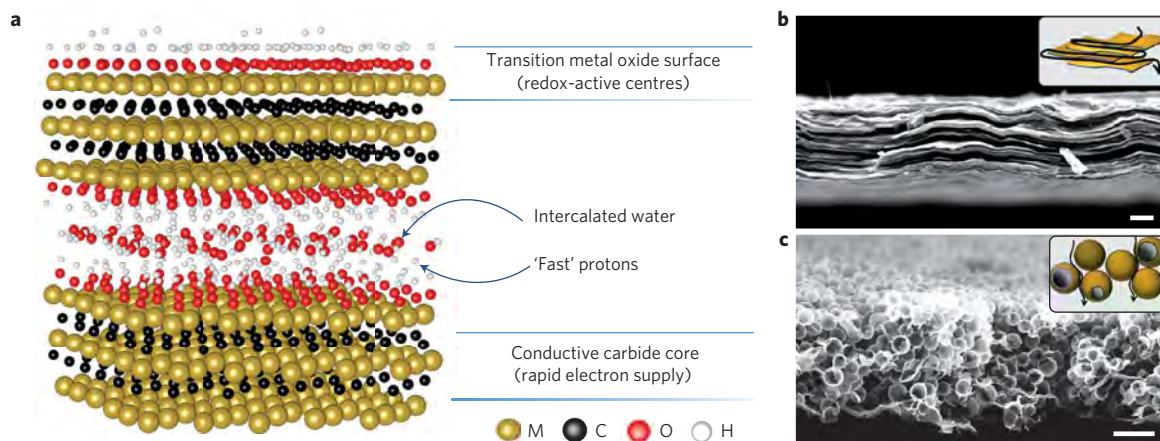
Figure 1 | MXene electrodes. a, Schematic illustration of MXene structure. MXenes possess excellent conductivity owing to a conductive carbide core along with transition metal oxide-like surfaces. Intercalated water molecules enable high accessibility of protons to the redox-active sites. **b**, SEM image of $Ti_3C_2T_x$ MXene hydrogel cross-section. **c**, SEM image of macroporous templated $Ti_3C_2T_x$ electrode cross-section. Scale bars, 5 µm. Insets in **b** and **c** show schematically the ionic current pathway in electrodes of different architectures.

almost linearly to changes in the titanium oxidation state[17]. It was also demonstrated that change in titanium oxidation state is accompanied by protonation of oxygen functional groups[18]. In a simplified view, the electrochemical reaction can be presented as:

$$Ti_3C_2O_x(OH)_yF_z + \delta\bar{e} + \delta H^+ \rightarrow Ti_3C_2O_{x-\delta}(OH)_{y+\delta}F_z \quad (1)$$
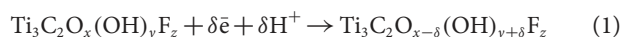
So far, the most promising electrochemical performance was demonstrated by MXenes produced via etching the MAX phase in LiF–HCl (ref. 14). According to NMR analysis, these synthetic conditions result in the following chemistry: $Ti_3C_2O_{0.84(6)}(OH)_{0.06(2)}F_{0.25(8)}$ (ref. 15). Assuming this chemical formula and 0.85 $\bar{e}$ redox reaction as per equation (1), the maximum theoretical capacity for the noted surface chemistry can be estimated using Faraday's law to be $\sim$615 C g^{-1}. Yet the maximum experimental values reported to date are 245 F g^{-1} or $\sim$135 C g^{-1} for a voltage window of 0.55 V (refs 14,17).

To analyse this discrepancy between theory and experiment, we performed electrochemical testing of a 90-nm-thick MXene film coating to minimize ion transport limitations stemming from the electrode architecture. In previous reports, testing of the capacitive performance was performed using platinum or gold current collectors[14,19], which can introduce limitations by catalysing water splitting within the potential range of interest. In the current work, glassy carbon electrodes were used as current collectors, instead. The advantage of the latter is their exceptional overpotential for hydrogen evolution reaction, which allows probing the intrinsic ability of different materials towards hydrogen evolution, making glassy carbon electrodes a primary current collector in the catalysis field[20]. When the $Ti_3C_2T_x$ MXene electrodes were tested in this configuration, the operation potential window was extended to 1 V (-1.1 to -0.1 V versus Hg/Hg$_2$SO$_4$) (Fig. 2a). Study of a 90-nm-thick electrodes revealed capacitance up to 450 F g^{-1} along with exceptional rate performance (Fig. 2b,d): capacitance decays only 27% following a 10^4-fold scan rate increase from 10 to 100,000 mV s^{-1} (Fig. 2c). Another characteristic feature of the charge storage process in $Ti_3C_2T_x$ is a small cathodic and anodic peak potential separation, ΔE_p (less than 50 mV for the scan rates up to 1,000 mV s^{-1}), indicating a highly reversible redox process at peak potential with a clear domain of quasi-equilibrium[2] (Fig. 2c); this is also confirmed by matching the capacitance extracted from voltammetry (CV) and electrochemical impedance spectroscopy (EIS) data for intercalation and deintercalation at the same potentials indicating the equilibrium nature of the process (Supplementary Fig. 1a,b).

It is important to note that, when 3 M H$_2$SO$_4$ was used as electrolyte in the current study, the higher concentration of protons resulted in slightly larger capacitance values and superior rate performance (Supplementary Fig. 1c–e), probably because conductivity of 3 M H$_2$SO$_4$ exceeds that of 1 M solution used in previous studies by almost an order of magnitude[21].

It is worth noting that although capacitive performance of 90-nm-thick film demonstrates an extent to which performance of $Ti_3C_2T_x$ can be improved, it has limited practical importance unless the noted above electrochemical response translates well for thicker practical electrodes[22]. We address realization of the enhanced electrochemical performance for the thick electrodes in the sections below.

Electrode design for high volumetric performance

A comparison of the performance of the 90 nm $Ti_3C_2T_x$ film with thicker (5 µm) electrodes[14] (Fig. 2d) shows a factor of two difference and suggests a decreasing accessibility of electrochemically active sites to ions with increasing thickness of planar electrodes. To test this conjecture, we prepared hydrogel electrodes[23] that provide delivery of electrolyte species in between MXene sheets (Supplementary Fig. 2). This approach was previously used to enhance performance of graphene in aqueous electrolytes[24] and also to enable access of bulky ionic liquid ions to electrochemically active sites of MXene[23]. As a result, a dramatic increase in gravimetric and volumetric performance over previous reports[14] was observed: capacitance of 380 F g^{-1} or 1,500 F cm^{-3} was measured at 2 mV s^{-1} for a 3 µm $Ti_3C_2T_x$ hydrogel electrode (1.2 mg cm^{-2} loading) over a potential window of 1 V. This translates to specific charge of 380 C g^{-1}, which is more than 3 times higher than our previous results[14] and corresponds to $\sim$65% from theoretical capacity. More importantly, these outstanding values translated well (for scan rates ranging from 2 to 20 mV s^{-1}) following increasing electrodes' mass loadings to practical ones of 5.3 and even 11.3 mg cm^{-2}. For instance, capacitance of 370 F g^{-1} or 1,500 F cm^{-3} was measured for a 13 µm $Ti_3C_2T_x$ hydrogel film electrode (5.3 mg cm^{-2}) at 2 mV s^{-1} (Fig. 2e and Fig. 3e and Supplementary Fig. 3b). These electrodes retained more than 90% of their capacitance after 10,000 cycles (Fig. 2f).

Typical EIS results are shown in Fig. 2g. The Nyquist plots collected at different applied reducing potentials are in a good agreement with the CV data (Fig. 2b and Supplementary Fig. 3). The Nyquist plots at potentials of -0.3 V and -0.5 V tend to overlap and are characterized by a low ion transport resistance and a sharp (almost vertical) rise of the imaginary component of impedance
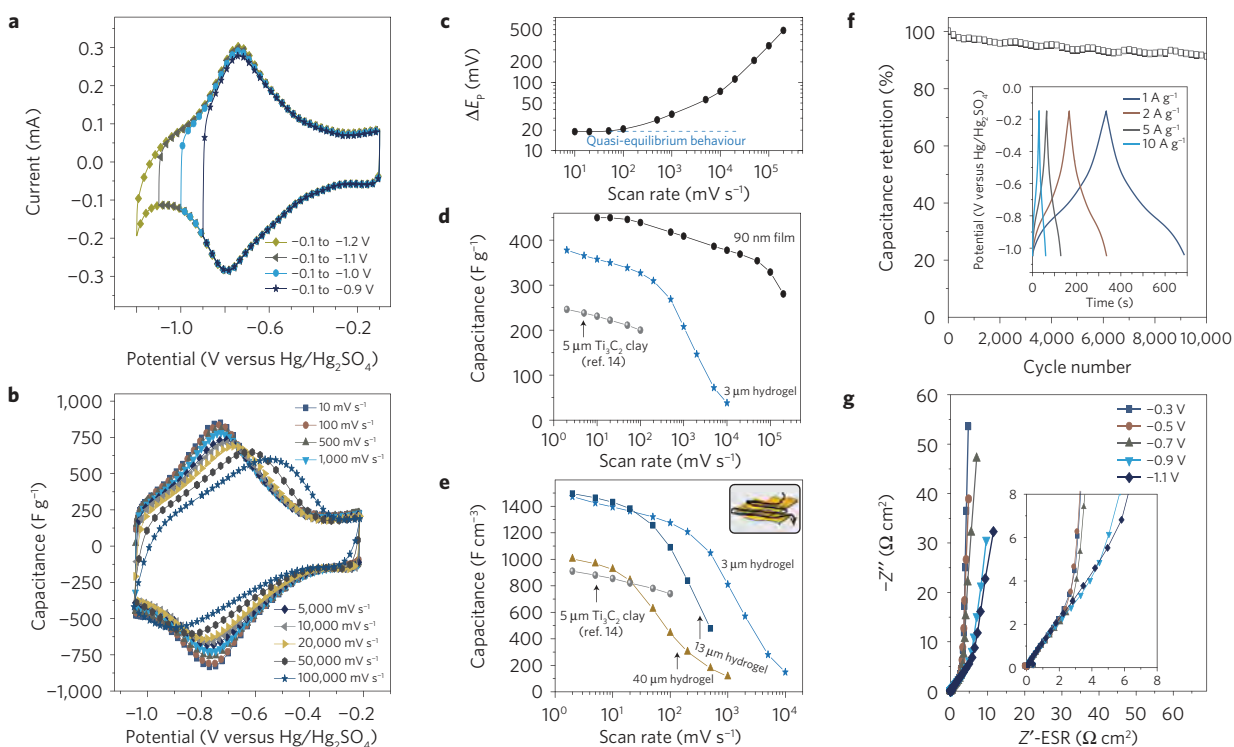
Figure 2 | Electrochemical performance of planar MXene electrodes. a, Cyclic voltammetry profiles for $Ti_3C_2T_x$ electrode collected at 5 mV s^{-1} in 3 M H_2SO_4 at different potential windows on a glassy carbon current collector. **b**, Cyclic voltammetry data collected at scan rates from 10 to 100,000 mV s^{-1} for a 90-nm-thick $Ti_3C_2T_x$ MXene. **c**, Peak separation, ΔE_p, for different scan rates extracted from CV analysis of 90 nm MXene film. The blue dashed line indicates the domain of the quasi-equilibrium. **d**, Gravimetric rate performance of a 90 nm $Ti_3C_2T_x$ film on glassy carbon current collector (black circles), and a 3-μm-thick hydrogel film electrode (blue stars), compared with the performance from ref. 14 of 5-μm-thick 'clay' electrode (grey spheres). **e**, Volumetric capacitance of 3-μm-thick (blue stars), 13-μm-thick (dark blue squares) and 40-μm-thick (gold triangles) hydrogel film electrode (mass loadings of 1.2 mg cm^{-2}, 5.3 mg cm^{-2} and 11.3 mg cm^{-2} accordingly) in 3 M H_2SO_4 compared with the performance from ref. 14 of 5-μm-thick 'clay' electrode (grey spheres) in 1 M H_2SO_4. The inset shows the ionic current pathway in a planar MXene electrode. **f**, Capacitance retention test of a 13 μm hydrogel film performed by galvanostatic cycling at 10 A g^{-1}. The inset depicts galvanostatic cycling profiles collected at 1, 2, 5 and 10 A g^{-1}. **g**, Electrochemical impedance spectroscopy data collected at different potentials for a vacuum-filtered $Ti_3C_2T_x$ hydrogel film (mass loading of 4.6 mg cm^{-2}). The inset shows the high-frequency range.

at low frequencies, demonstrating the capacitive behaviour of the electrode. As can be seen from both EIS (Fig. 2g) and CV profiles collected at different scan rates (Fig. 2b and Supplementary Fig. 3), this potential region corresponds to a relatively low capacitance originating from non-diffusion-limited processes. A slight increase of the 45-degree linear part (related to ion transport resistance) and a less steep slope of the Nyquist plot in the low-frequency range at −0.7 V were followed by a large increase of the 45-degree linear part at −0.9 V and −1.1 V. This correlates with the appearance of redox peaks in the CVs (Fig. 2b and Supplementary Fig. 3b) associated with a pseudocapacitive mechanism. There are clear diffusion limitations that translate into substantial capacitance decrease at potentials below −0.4 V with increasing scan rate (Supplementary Fig. 3). Further increase in ion transport resistance for EIS collected at −1.1 V may originate from the onset of hydrogen evolution during exposure for 30 min (see the H_2 evolution 'tail' features in the CVs in Fig. 2a and Supplementary Fig. 3a).

Electrode design for high-rate performance

Pseudocapacitive materials are usually tested at moderate charge–discharge rates, namely between those of batteries and EDLCs. The electrochemical performance of MXenes at high rates remained unexplored, but previous reports demonstrated good rate handling ability up to 100 mV s^{-1} for electrodes having areal density in the range from 1 to 5 mg cm^{-2} (refs 14,16,25). As shown in Fig. 2d, thin $Ti_3C_2T_x$ films deliver an exceptionally high-rate performance, yet

when the $Ti_3C_2T_x$ hydrogel electrode was subjected to charging rates above 200 mV s^{-1}, a rapid decrease in gravimetric and volumetric capacitance was observed.

The planar 'paper' electrode architecture with horizontal alignment of MXene flakes, which is formed during vacuum-assisted filtration of the colloidal solution (Fig. 1b), results in electrode density approaching 4 g cm^{-3}. This leads to a high volumetric capacitance, but limits high-rate charge transfer and impedes ion transport towards redox-active sites (Fig. 2g).

Electrode architectures with macroporosity[26,27] as well as decreased pore tortuosity[28] were shown to be efficient to address this problem. Herein, we used templating with polymethyl methacrylate (PMMA) microspheres[29] to create electrodes with open structure (Fig. 1c). In these electrodes—characterized by 1–2-μm-diameter macropores with submicrometre MXene wall thicknesses—the ion transport lengths are greatly reduced. X-ray diffraction data suggested less ordering of flakes in macroporous MXene (MP-MXene) electrodes with only the (0002) peak appearing, in contrast to a set of (000l) peaks for MXene paper with well-aligned sheets (Supplementary Fig. 4). Transmission electron microscopy (TEM) analysis of the edge of an individual $Ti_3C_2T_x$ flake confirmed the presence of single-layer flakes (Supplementary Fig. 5a). Supplementary Fig. 5b shows the connection point of two $Ti_3C_2T_x$ hollow spheres. Each sphere consists of a few monolayers with some flakes shared between each of them, providing a good connection and mechanical robustness (Supplementary Figs 5b and 6).
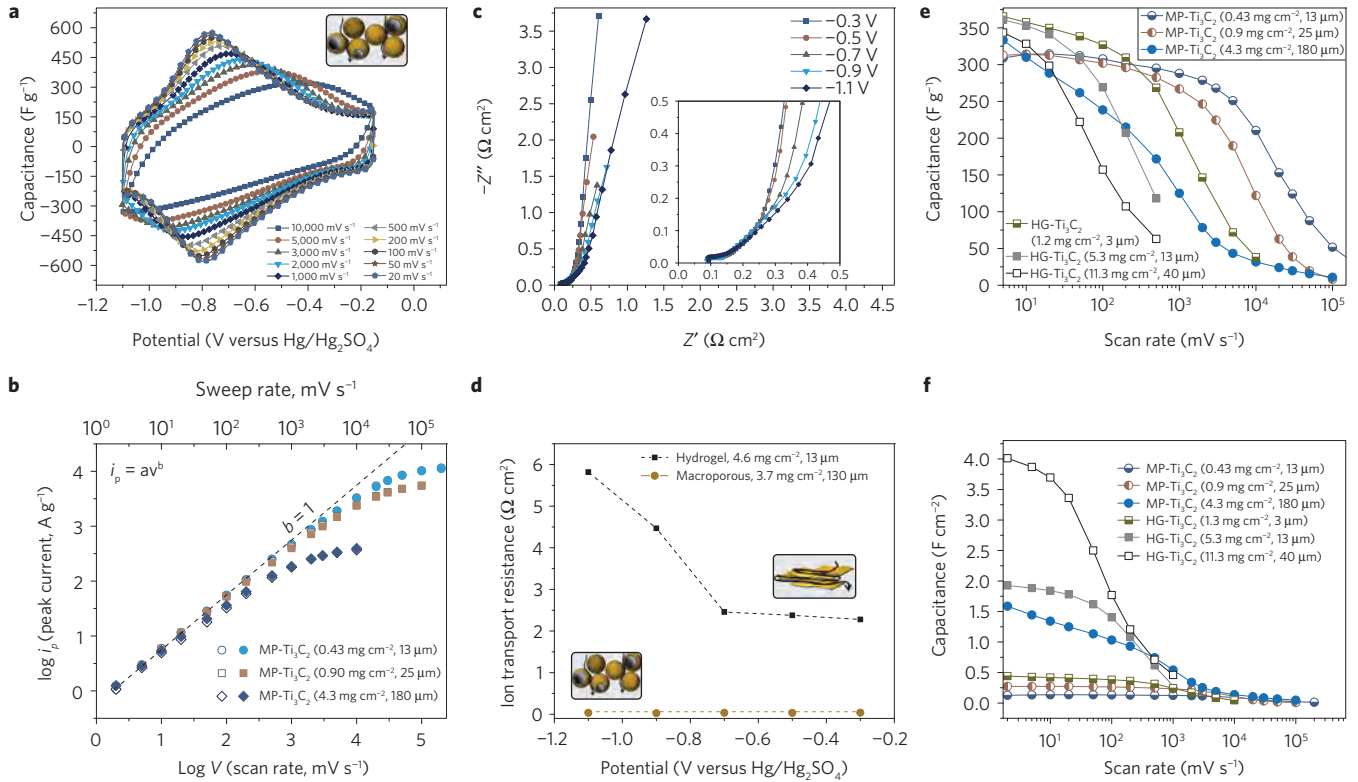
Figure 3 | Electrochemical performance of macroporous Ti₃C₂Tₓ electrodes. a, Cyclic voltammetry profiles of a macroporous 13-μm-thick film with a 0.43 mg cm⁻² loading collected in 3 M H₂SO₄ at scan rates from 20 to 10,000 mV s⁻¹. The inset shows schematically macroporous electrode architecture and ionic current pathways in it. **b**, Determination of the slope, *b*, for the logarithm of anodic (open symbols) and cathodic (filled symbols) peak current versus logarithm of scan rate for macroporous films with different mass loadings from 0.45 to 4.5 mg cm⁻². Capacitive storage is indicated by *b* = 1 while *b* = 0.5 is characteristic for diffusion-limited processes. **c**, Electrochemical impedance spectroscopy data collected at different potentials for a macroporous film (3.7 mg cm⁻² loading). **d**, Comparison of ion transport resistance for hydrogel (black squares) and macroporous (yellow circles) electrodes extracted from EIS collected at different applied potentials. The insets show schematically the ionic current pathway in hydrogel (top) and macroporous (bottom) electrodes. **e,f**, Rate performance of MXene films with different preparation methods and mass loadings represented in gravimetric (**e**) and areal (**f**) capacitance.

Electrochemical studies of these macroporous electrodes revealed exceptional rate handling ability for a pseudocapacitive material (Fig. 3a,e), with gravimetric capacitance of 310 F g⁻¹ at a scan rate of 10 mV s⁻¹ (0.135 F cm⁻²); 210 F g⁻¹ (0.090 F cm⁻²) at 10 V s⁻¹ and 100 F g⁻¹ (0.043 F cm⁻²) at 40 V s⁻¹ for a 13-μm-thick film, surpassing some of the best reported results[30,31]. To shed light on the charge storage kinetics, an analysis of peak current dependence on the scan rate was carried out. Assuming power-law dependence of the current, *i*, on scan rate, *ν*:

$$i_p = a\nu^b \tag{2}$$

where *a* and *b* are variables, and a plot of log *i* versus log *ν* should result in a straight line with a slope equal to *b* (Fig. 3b). The *b*-value provides important information on the charge storage kinetics: *b* = 1 indicates capacitive storage, while *b* = 0.5 is characteristic for diffusion-limited processes[32]. Herein for the 13 μm macroporous film, *b* was ≈1 up to scan rates of 3 V s⁻¹ (light blue symbols in Fig. 3b). For a 25-μm-thick macroporous electrode *b* was ≈1 up to scan rates of 2 V s⁻¹ (Fig. 3b), which reflected in excellent rate performance of the sample with capacitance of 280 F g⁻¹ (0.23 F cm⁻²) at 1 V s⁻¹ and 120 F g⁻¹ (0.10 F cm⁻²) at 10 V s⁻¹. Even a 180-μm-thick film demonstrated capacitance of 125 F g⁻¹ (0.54 F cm⁻²) at 1 V s⁻¹ and 32 F g⁻¹ (0.14 F cm⁻²) at 10 V s⁻¹ (Fig. 3b,e,f). Corresponding CV profiles for 25 μm and 180 μm samples collected at different scan rates are shown in Supplementary Fig. 7a,b, respectively. EIS data collected at different

potentials for the thick macroporous electrode with 3.7 mg cm⁻² weight loading revealed a significant decrease in ion transport resistance of 0.04 Ω cm² across all potentials for this electrode architecture when compared with hydrogel samples of comparable weight loading (Fig. 3c,d). It is important to mention that the open structure of the MP electrodes results in a lower electrode density (~0.35 g cm⁻³) and therefore hydrogel-type electrodes should be used for high volumetric performance, since they possess a high density (~4 g cm⁻³).

It is worth noting that exceptional high-rate performance is not unique to Ti₃C₂Tₓ MXene. As shown in Supplementary Fig. 8, only slight distortions of the CVs with increased scan rate are observed for a 30-μm-thick macroporous Mo₂CTₓ electrode, with a capacitance of 100 F g⁻¹ at 10 V s⁻¹. Given that more than 15 MXenes have been reported in the literature[13] and the large compositional variability of the MAX phase[33] precursors, it is reasonable to expect that other MXenes may perform equally well as, or better than, Ti₃C₂Tₓ and Mo₂CTₓ. Moreover, these design strategies also enabled exceptional areal capacitances; that is, for 40-μm-thick hydrogel electrodes 4 F cm⁻² is achieved at 5 mV s⁻¹ (Fig. 3e); for a macroporous electrode with mass loading of 4.3 mg cm⁻², areal capacitance above 0.5 F cm⁻² was maintained at scan rates up to 1 V s⁻¹.

Conclusions
In summary, we have demonstrated how different electrode design strategies can push MXene capacitance closer to its theoretical

limit. Using glassy carbon current collectors, the working potential window was extended to 1 V in 3 M H_2SO_4 electrolyte. We also show that the extended voltage window is not unique to glassy carbon, but is also achieved when other current collectors, such as graphite (Supplementary Fig. 9b) or Ti foil (Supplementary Fig. 9c), are used. Macroporous electrode architectures enabled outstanding capacitance retention even at charge–discharge rates above $1\,V\,s^{-1}$: $210\,F\,g^{-1}$ at $10\,V\,s^{-1}$ and $100\,F\,g^{-1}$ at $40\,V\,s^{-1}$, surpassing the best carbon supercapacitors known[34]. Hydrogel electrodes demonstrated exceptional volumetric capacitance up to $1,500\,F\,cm^{-3}$ and areal capacitance up to $4\,F\,cm^{-2}$, exceeding state-of-the-art supercapacitor materials[30,31,34–37]. This study shows that pseudocapacitive materials can be used for energy harvesting and storage at rates exceeding $10\,V\,s^{-1}$, and probably higher rates can be achieved after further optimization of material composition and architecture, opening new exciting opportunities in the fields of electrochemical energy harvesting, conversion and storage.

Methods

Synthesis of $Ti_3C_2T_x$. A mixture of hydrochloric acid (HCl) and lithium fluoride (LiF) was used to synthesize multilayer $Ti_3C_2T_x$ from Ti_3AlC_2, which were synthesized similarly to a previous report[14]. Specifically, 2 g of LiF was added to 40 ml of 9 M HCl (Fisher, Technical), followed by the slow addition of 2 g of Ti_3AlC_2 (ice bath). After etching for 24 h at 35 °C, the multilayer $Ti_3C_2T_x$ was washed and centrifuged with deionized water until the supernatant reached a pH value ≈6. Next, the MXene powders were again mixed with deionized water and bath sonicated for 1 h, while bubbling Ar gas through the mixture. The sonication bath water with cooled with ice. Afterwards, the mixture was centrifuged for 1 h at 3,500 r.p.m. (2,301g). The resultant dark supernatant was a colloidal suspension of few-layer $Ti_3C_2T_x$ used to fabricate various $Ti_3C_2T_x$ electrodes (see below).

Synthesis of Mo_2CT_x. Molybdenum carbide MXene (Mo_2CT_x) was synthesized by immersing Mo_2Ga_2C in hydrofluoric acid (HF), according to a recent paper[16]. The multilayer Mo_2CT_x powders were washed with deionized water and centrifuged repeatedly to neutral pH. The powders were then mixed with tetrabutylammonium hydroxide (TBAOH; Acros Organics, 40 wt% in water), for 2 h under continuous stirring at room temperature. The mixture was centrifuged for 5 min at 5,000 r.p.m. (4,696g), and the supernatant was decanted. The intercalated Mo_2CT_x sediment was rinsed with deionized water three times to remove residual TBAOH. The sediment was then mixed with deionized water and vigorously shaken in a vortex mixer to delaminate the Mo_2CT_x into few-layer Mo_2CT_x. After centrifugation for 1 h at 5,000 r.p.m. (4,696g), the supernatant was separated from the sediment and used without further preparation to make various Mo_2CT_x electrodes (see below).

Preparation of Ti_3C_2 'paper' electrodes. A $Ti_3C_2T_x$ colloidal solution was vacuum-filtered through nanoporous polypropylene membrane (Celgard 3501, Celgard LLC) to make MXene 'paper' electrodes (VF-MXene). Once all of the water passed through the filter, the films were air-dried for several hours, before being peeled off the membrane and then used for electrochemical testing. Resulting electrode density values fall in the range from 3.7 to $4\,g\,cm^{-3}$.

Preparation of macroporous MXene electrodes. To synthesize hollow MXene spheres we first fabricated poly(methyl methacrylate) (PMMA) spheres following the process described in ref. 38. In short, a radical initiator, azoisobutyronitrile (Sigma-Aldrich), and a stabilizer, poly(vinyl pyrrolidone) (Sigma-Aldrich), were dissolved in methanol with a concentration of 0.1 and 4.0 wt%, respectively, at room temperature. The solution was purged with Ar for 10 min to remove oxygen. After that, methyl methacrylate monomer (MMA, Sigma-Aldrich) was added, at a concentration of 10 wt%. The mixture was stirred at 55 °C for 24 h. Then, the white PMMA spheres were collected by centrifugation and washed with methanol. A colloidal solution of PMMA spheres was prepared by dispersing PMMA spheres in ethanol by sonication, at a concentration of $10\,mg\,ml^{-1}$. Colloidal solutions of $Ti_3C_2T_x$ ($2\,mg\,ml^{-1}$) and PMMA spheres ($10\,mg\,ml^{-1}$) were mixed together while stirring. The mass ratio of $Ti_3C_2T_x$ to PMMA spheres was controlled at 1:4. The mixture was sonicated for 10 min to ensure the uniform dispersion of $Ti_3C_2T_x$ flakes and PMMA spheres in the solution. The mixture was filtered through a polypropylene membrane (3501 Coated PP, Celgard LL) to yield a film. This film was dried in air at room temperature for 10 min and peeled off from the polypropylene membrane, yielding a flexible freestanding $Ti_3C_2T_x$/PMMA composite film. This composite film was annealed at 400 °C under flowing Ar for 1 h to burn out the PMMA spheres, leaving a macroporous $Ti_3C_2T_x$ film. The film thickness was controlled by varying the amount of $Ti_3C_2T_x$ flakes used. Macroporous Mo_2CT_x films were prepared in a similar

manner. Resulting electrode density values fall in the range from 0.25 to $0.4\,g\,cm^{-3}$. Density of 0.35 to $0.4\,g\,cm^{-3}$ was characteristic of electrodes with small to intermediate thickness (<30 μm), while thicker electrodes (150–200 μm) possessed the density of 0.25 to $0.3\,g\,cm^{-3}$.

Preparation of $Ti_3C_2T_x$ hydrogels. $Ti_3C_2T_x$ hydrogel films were prepared by vacuum filtration of a delaminated $Ti_3C_2T_x$ colloidal solution. It should be noted that the vacuum was disconnected immediately once there was no free $Ti_3C_2T_x$ colloidal solution on the filtrate. Afterwards, the obtained hydrogel film was immersed in acetone and carefully peeled off from the filter membrane. After immersing in the electrolyte for 72 h, the hydrogel film was then used for electrochemical characterizations directly. Resulting electrode density values fall in the range from 2.8 to $4.3\,g\,cm^{-3}$. Thinner electrodes (1 to 15 μm thick) possessed the highest density of $\sim4\,g\,cm^{-3}$, while thicker ones (~40 μm) showed the lowest density of $\sim2.8\,g\,cm^{-3}$. This can be explained by better alignment of MXene flakes in thinner electrodes.

Electrochemical measurements. All electrochemical tests were performed using a VMP3 potentiostat (Biologic). Cyclic voltammetry was conducted in three-electrode plastic Swagelok cells. MXene electrode on glassy carbon current collector was used as a working electrode and overcapacitive activated carbon was used as a counter electrode. The reference electrodes were either Hg/Hg_2SO_4 in saturated K_2SO_4 or Ag/AgCl in 1 M KCl. After initially pre-cycling the electrodes at $20\,mV\,s^{-1}$ the cells were tested from scan rates of $2\,mV\,s^{-1}$ to $100,000\,mV\,s^{-1}$. Galvanostatic cycling was performed at current densities from 1 to $100\,A\,g^{-1}$. The same 3-electrode cell configuration described above was used for electrochemical impedance spectroscopy (EIS) in the 100 mHz to 100 kHz range using a potential amplitude of 10 mV. EIS spectra were collected at various potentials and were recorded versus Hg/Hg_2SO_4 reference electrode after holding at each potential for 0.5 h (Fig. 3a). For thick hydrogel samples, the ESR (equivalent series resistance) was subtracted from the real part resistance as shown on the x axis, to eliminate the effect of resistance originating from the Hg/Hg_2SO_4 reference electrode, which may also vary with the potential. The ion transport resistance at each potential was then calculated from the difference of the knee frequency resistance and the ESR, and plotted versus potential (Fig. 3d).

Capacitance calculations. The capacitance was calculated by integration of current with respect to time:

$$C = \frac{\int_0^{V/s} |j|\,\mathrm{d}t}{V} \tag{3}$$

where C is the gravimetric capacitance ($F\,g^{-1}$), j is the gravimetric current density ($A\,g^{-1}$), s is the scan rate ($V\,s^{-1}$), and V is the potential window (V). To calculate the volumetric and areal capacitances, the gravimetric capacitance was multiplied by the volumetric ($g\,cm^{-3}$) or areal ($g\,cm^{-2}$) density of the electrode.

Characterization of structure and properties. X-ray diffraction (XRD) patterns of MXene films were obtained using a powder diffractometer (SmartLab, Rigaku Corp. or D4 ENDEAVOR, Bruker) using Cu $K\alpha_1$ radiation. A scanning electron microscope, (SEM; Zeiss Supra 50VP, Carl Zeiss SMT AG or JSM-6510LV, JEOL), equipped with an energy-dispersive X-ray spectroscope (Oxford EDS), was used to characterize the microstructure and measure the electrode thicknesses. A JEM-2100 (JEOL) transmission electron microscope (TEM) was used to analyse the MXene flakes using an accelerating voltage of 200 kV. Samples for TEM observation were prepared by dropping two drops of the MXene dispersion in water onto a lacey carbon-coated copper grid (Electron Microscopy Sciences) and air-dried.

Characterization of macroporous electrodes. Synthesis of the PMMA resulted in spherical particles 1.7 ± 0.3 μm in diameter, as shown in Supplementary Fig. 5a. When the PMMA spheres were mixed with colloidal Ti_3C_2 flakes, the former acted as templates for the latter to wrap around into a MXene/PMMA composite. After heating the composite at 400 °C under Ar flow, the PMMA spheres evaporated, resulting in hollow $Ti_3C_2T_x$ spheres of roughly the same size as the PMMA particles (Supplementary Fig. 5b). The same method was used to produce Mo_2CT_x hollow spheres of the same size. Micrographs of the macroporous $Ti_3C_2T_x$ and Mo_2CT_x films' cross-sections are shown in Supplementary Fig. 5c,d.

The XRD patterns of a vacuum-filtered $Ti_3C_2T_x$ film (Supplementary Fig. 4a) show only the broad (000l) MXene peaks, confirming that the synthesis was successful. The d_{0002} peak at 6.6° 2θ corresponds to a c-lattice parameter of 26.8 Å, which is close to typical values found in the literature[39]. After annealing the PMMA/Ti_3C_2 mixture at 400 °C, the c-lattice parameter remained unchanged, but all (000l) peaks become significantly broader such that the higher order basal reflections were longer visible. More importantly, the absence of reflections corresponding to PMMA at 13° and 30° 2θ in the XRD pattern[38] of the macroporous films confirmed their full removal. Similarly, the XRD pattern of a vacuum-filtered Mo_2CT_x film (Supplementary Fig. 4b) shows broad (000l)

peaks, in agreement with previous reports[16]. After annealing away the PMMA spheres however, the (0002) peak experiences significant broadening and a slight upshift in angle. These observations may reflect the vaporization and deintercalation of residual tetrabutylammonium cations.

Processing control for hydrogel films. The thicknesses and mass loadings of the hydrogel films were controlled by starting with different volumes of $Ti_3C_2T_x$ colloidal solutions during vacuum filtration. However, as mentioned above, the water from the $Ti_3C_2T_x$ colloidal solutions was not completely removed following drying. Therefore, the mass loadings and thicknesses of the hydrogel films were only precisely measured after the electrochemical tests. Specifically, the tested films were washed with deionized water and ethanol to remove the electrolyte, and then dried in a vacuum oven for more than 24 h. Lastly, the mass and thicknesses of the dried films were measured with a microbalance and SEM, respectively.

Data availability. The data that support the plots within this paper and other findings of this study are available from the corresponding authors on request.

References

1. Lukatskaya, M. R., Dunn, B. & Gogotsi, Y. Multidimensional materials and device architectures for future hybrid energy storage. *Nat. Commun.* **7,** 12647 (2016).
2. Conway, B. *Electrochemical Supercapacitors: Scientific Fundamentals and Technological Applications* (Kluwer Academic/Plenum, 1999).
3. Simon, P. & Gogotsi, Y. Materials for electrochemical capacitors. *Nat. Mater.* **7,** 845–854 (2008).
4. Sugimoto, W., Iwata, H., Yokoshima, K., Murakami, Y. & Takasu, Y. Proton and electron conductivity in hydrous ruthenium oxides evaluated by electrochemical impedance spectroscopy: the origin of large capacitance. *J. Phys. Chem. B* **109,** 7330–7338 (2005).
5. Zheng, J. P., Cygan, P. J. & Jow, T. R. Hydrous ruthenium oxide as an electrode material for electrochemical capacitors. *J. Electrochem. Soc.* **142,** 2699–2703 (1995).
6. Sassoye, C. *et al.* Block-copolymer-templated synthesis of electroactive RuO_2-based mesoporous thin films. *Adv. Funct. Mater.* **19,** 1922–1929 (2009).
7. Hu, C.-C., Chang, K.-H., Lin, M.-C. & Wu, Y.-T. Design and tailoring of the nanotubular arrayed architecture of hydrous RuO_2 for next generation supercapacitors. *Nano Lett.* **6,** 2690–2695 (2006).
8. Toupin, M., Brousse, T. & Bélanger, D. Charge storage mechanism of MnO_2 electrode used in aqueous electrochemical capacitor. *Chem. Mater.* **16,** 3184–3190 (2004).
9. Brezesinski, T., Wang, J., Tolbert, S. H. & Dunn, B. Ordered mesoporous [alpha]-MoO_3 with iso-oriented nanocrystalline walls for thin-film pseudocapacitors. *Nat. Mater.* **9,** 146–151 (2010).
10. Come, J. *et al.* Electrochemical kinetics of nanostructured Nb_2O_5 electrodes. *J. Electrochem. Soc.* **161,** A718–A725 (2014).
11. Augustyn, V. *et al.* High-rate electrochemical energy storage through Li^+ intercalation pseudocapacitance. *Nat. Mater.* **12,** 518–522 (2013).
12. Choi, D., Blomgren, G. E. & Kumta, P. N. Fast and reversible surface redox reaction in nanocrystalline vanadium nitride supercapacitors. *Adv. Mater.* **18,** 1178–1182 (2006).
13. Naguib, M., Mochalin, V. N., Barsoum, M. W. & Gogotsi, Y. MXenes: a new family of two-dimensional materials. *Adv. Mater.* **26,** 992–1004 (2014).
14. Ghidiu, M., Lukatskaya, M. R., Zhao, M.-Q., Gogotsi, Y. & Barsoum, M. W. Conductive two-dimensional titanium carbide 'clay' with high volumetric capacitance. *Nature* **516,** 78–81 (2014).
15. Hope, M. A. *et al.* NMR reveals the surface functionalisation of Ti_3C_2 MXene. *Phys. Chem. Chem. Phys.* **18,** 5099–5102 (2016).
16. Halim, J. *et al.* Synthesis and characterization of 2D molybdenum carbide (MXene). *Adv. Funct. Mater.* **26,** 3118–3127 (2016).
17. Lukatskaya, M. R. *et al.* Probing the mechanism of high capacitance in 2D titanium carbide using *in situ* X-ray absorption spectroscopy. *Adv. Energy Mater.* **5,** 1500589 (2015).
18. Hu, M. *et al.* High-capacitance mechanism for $Ti_3C_2T_x$ MXene by *in situ* electrochemical raman spectroscopy investigation. *ACS Nano* **10,** 11344–11350 (2016).
19. Lukatskaya, M. R. *et al.* Cation intercalation and high volumetric capacitance of two-dimensional titanium carbide. *Science* **341,** 1502–1505 (2013).
20. Benck, J. D., Pinaud, B. A., Gorlin, Y. & Jaramillo, T. F. Substrate selection for fundamental studies of electrocatalysts and photoelectrodes: inert potential windows in acidic, neutral, and basic electrolyte. *PLoS ONE* **9,** e107942 (2014).
21. Darling, H. E. Conductivity of sulfuric acid solutions. *J. Chem. Eng. Data* **9,** 421–426 (1964).
22. Gogotsi, Y. & Simon, P. True performance metrics in electrochemical energy storage. *Science* **334,** 917–918 (2011).
23. Lin, Z. *et al.* Capacitance of $Ti_3C_2T_x$ MXene in ionic liquid electrolyte. *J. Power Sources* **326,** 575–579 (2016).
24. Yang, X., Cheng, C., Wang, Y., Qiu, L. & Li, D. Liquid-mediated dense integration of graphene materials for compact capacitive energy storage. *Science* **341,** 534–537 (2013).
25. Mashtalir, O. *et al.* The effect of hydrazine intercalation on structure and capacitance of 2D titanium carbide (MXene). *Nanoscale* **8,** 9128–9133 (2016).
26. Li, Y. *et al.* Synthesis of hierarchically porous sandwich-like carbon materials for high-performance supercapacitors. *Chem. Eur. J.* **22,** 16863–16871 (2016).
27. Zhu, C. *et al.* Supercapacitors based on three-dimensional hierarchical graphene aerogels with periodic macropores. *Nano Lett.* **16,** 3448–3456 (2016).
28. Yoo, J. J. *et al.* Ultrathin planar graphene supercapacitors. *Nano Lett.* **11,** 1423–1427 (2011).
29. Chen, C.-M. *et al.* Macroporous 'bubble' graphene film via template-directed ordered-assembly for high rate supercapacitors. *Chem. Commun.* **48,** 7149–7151 (2012).
30. Lang, X.-Y. *et al.* Ultrahigh-power pseudocapacitors based on ordered porous heterostructures of electron-correlated oxides. *Adv. Sci.* **3,** 1500319 (2016).
31. El-Kady, M. F. *et al.* Engineering three-dimensional hybrid supercapacitors and microsupercapacitors for high-performance integrated energy storage. *Proc. Natl Acad. Sci. USA* **112,** 4233–4238 (2015).
32. Lindström, H. *et al.* Li^+ ion insertion in TiO_2 (Anatase). 2. Voltammetry on nanoporous films. *J. Phys. Chem. B* **101,** 7717–7722 (1997).
33. Barsoum, M. W. The $M_{N+1}AX_N$ phases: a new class of solids: thermodynamically stable nanolaminates. *Prog. Solid State Chem.* **28,** 201–281 (2000).
34. Pech, D. *et al.* Ultrahigh-power micrometre-sized supercapacitors based on onion-like carbon. *Nat. Nanotech.* **5,** 651–654 (2010).
35. Acerce, M., Voiry, D. & Chhowalla, M. Metallic 1T phase MoS_2 nanosheets as supercapacitor electrode materials. *Nat. Nanotech.* **10,** 313–318 (2015).
36. Zhu, M. *et al.* Highly flexible, freestanding supercapacitor electrode with enhanced performance obtained by hybridizing polypyrrole chains with MXene. *Adv. Energy Mater.* **6,** 1600969 (2016).
37. Zhao, X. *et al.* Incorporation of manganese dioxide within ultraporous activated graphene for high-performance electrochemical capacitors. *ACS Nano* **6,** 5404–5412 (2012).
38. Shen, S., Sudol, E. D. & El-Aasser, M. S. Control of particle size in dispersion polymerization of methyl methacrylate. *J. Polym. Sci. A* **31,** 1393–1402 (1993).
39. Ling, Z. *et al.* Flexible and conductive MXene films and nanocomposites with high capacitance. *Proc. Natl Acad. Sci. USA* **111,** 16676–16681 (2014).

Acknowledgements

Author contributions

M.R.L. and Y.G. planned the study. S.K., M.R.L., Z.L. and N.S. conducted electrochemical testing. Z.L. and S.K. performed XRD and SEM analysis. M.-Q.Z., Z.L. and J.H. synthesized MXenes and fabricated electrodes. M.-Q.Z. performed TEM analysis. Y.G., P.S., M.R.L., M.D.L., P.-L.T. and M.W.B. supervised the research and discussed the results.

Additional information

Competing interests

Ultra-high-rate pseudocapacitive energy storage in two-dimensional transition metal carbides

Supplementary Figure 1 | Electrochemical performance of thin Ti₃C₂Tₓ films. a, Cyclic voltammetry profile (line) with over-imposed values of capacitance extracted from EIS at different intercalation (red spheres) and deintercalation (blue spheres) potentials. **b**, EIS data (Nyquist plot) collected at 0 V vs. Ag/AgCl on the intercalation (filled spheres) and deintercalation (hollow squares) branches. **c**, Bode plot collected at 0 V vs. Ag/AgCl. **c**, Gravimetric rate performance extracted from cyclic voltammetry profiles of a 90 nm film on glassy carbon electrode in 1M (black squares) and 3M (red circles) H₂SO₄. **d**, Cyclic voltammetry profiles collected at 50,000 mV s⁻¹ in 1M (black) and 3M H₂SO₄ (red).
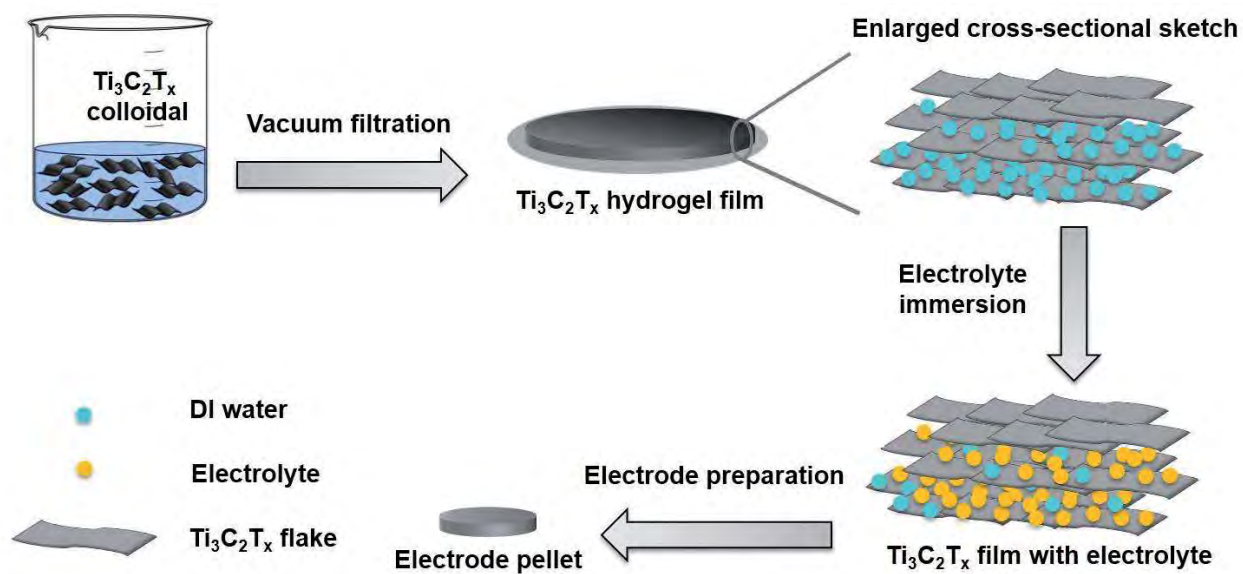
Supplementary Figure 2| Schematic illustration of Ti$_3$C$_2$T$_x$/H$_2$SO$_4$ hydrogel preparation procedure. Ti$_3$C$_2$T$_x$ colloidal solution was taken for vacuum filtration to prepare the Ti$_3$C$_2$T$_x$ hydrogel film. The obtained hydrogel film was then immersed in 3 M H$_2$SO$_4$ electrolyte to replace the water and increase/ensure accessibility of MXene surface to the electrolytes. Electrode pellet was punched out from the Ti$_3$C$_2$T$_x$ film after electrolyte immersion for more than 24 h.
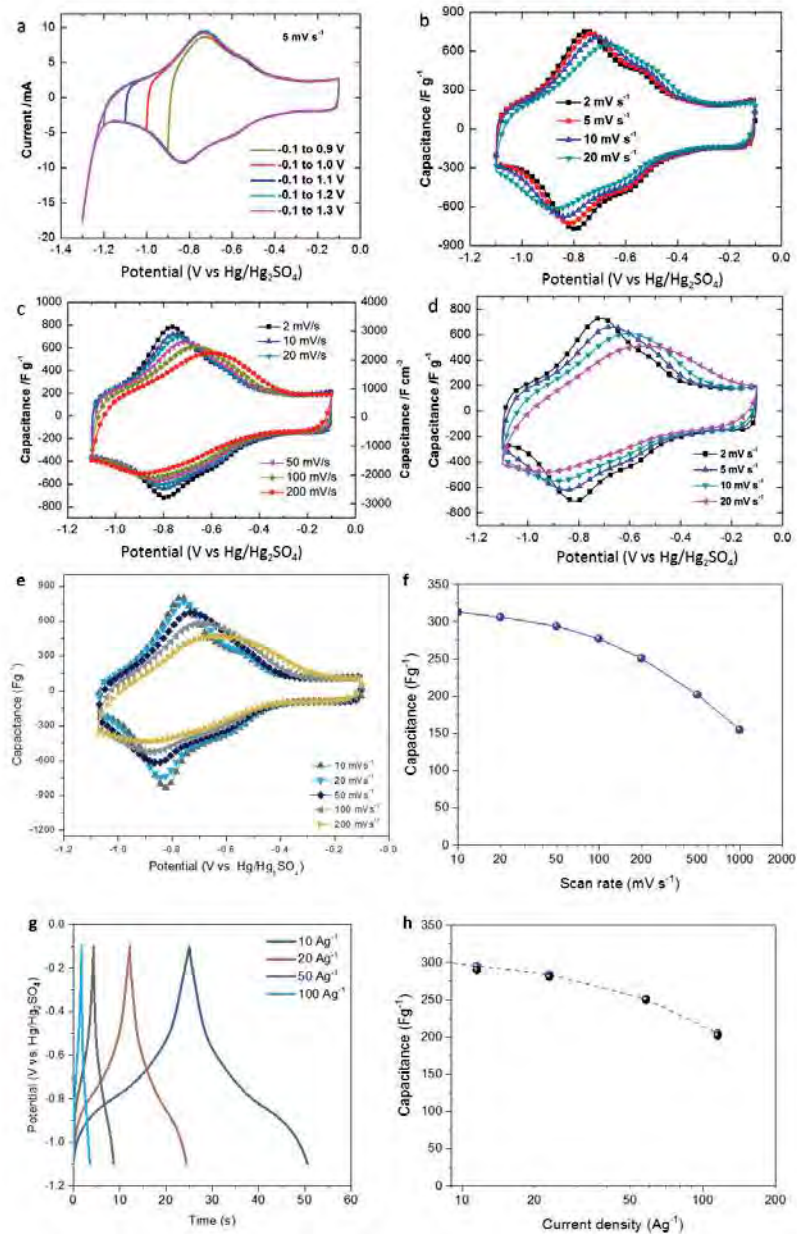
Supplementary Figure 3 | Electrochemical performance of Ti₃C₂Tₓ hydrogel films. **a**, Cyclic voltammetry profiles collected at 5 mVs⁻¹ in different potential ranges (active material mass loading of 5.3 mg/cm², 13 μm thick). **b**, Cyclic voltammetry profiles collected at scan rates from 2 to 20 mV s⁻¹ (active material mass loading of 5.3 mg/cm², 13 μm thick). **c**, Cyclic voltammetry profiles collected at scan rates from 2 to 200 mV s⁻¹ (active material mass loading of 1.2 mg/cm², 3 μm thick). **d,** Cyclic voltammetry profiles collected at scan rates from 2 to 20 mV s⁻¹ (active material mass loading of 11.3 mg/cm², 40 μm thick). **e-h:** Rate performance of a hydrogel sample with mass loading of 2.65 mg/cm²: **e,** Cyclic voltammetry profiles collected at scan rates from 10 to 200 mV s⁻¹. **f,** Gravimetric rate performance (from CV): capacitance vs. scan rate. **g,** Galvanostatic cycling profiles collected at 10, 20, 50 and 100 Ag⁻¹. **e,** Gravimetric rate performance (from GCPL): capacitance vs. charge/discharge current density.
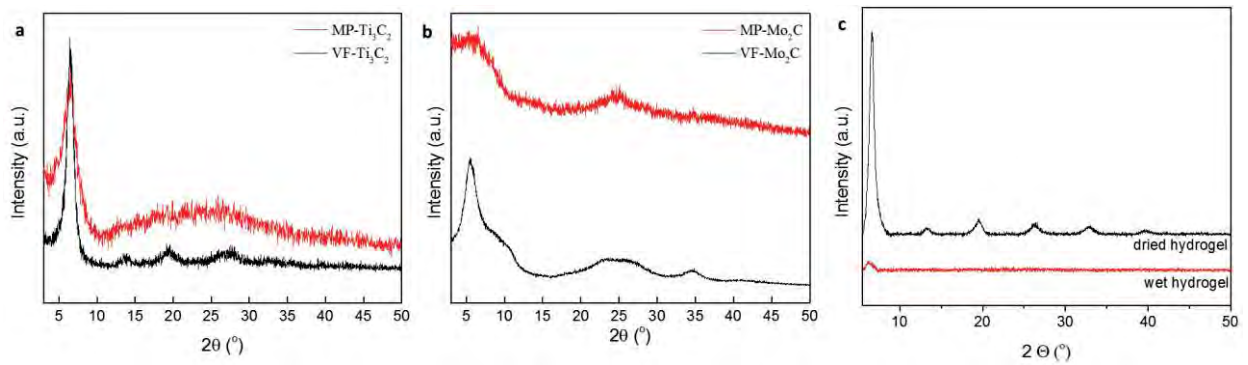
Supplementary Figure 4 | X-ray diffractograms of a, $Ti_3C_2T_x$ MXene macroporous and vacuum-filtered freestanding films. **b,** Mo_2CT_x MXenes macroporous and vacuum-filtered freestanding films. **c,** dry and wet hydrogel.
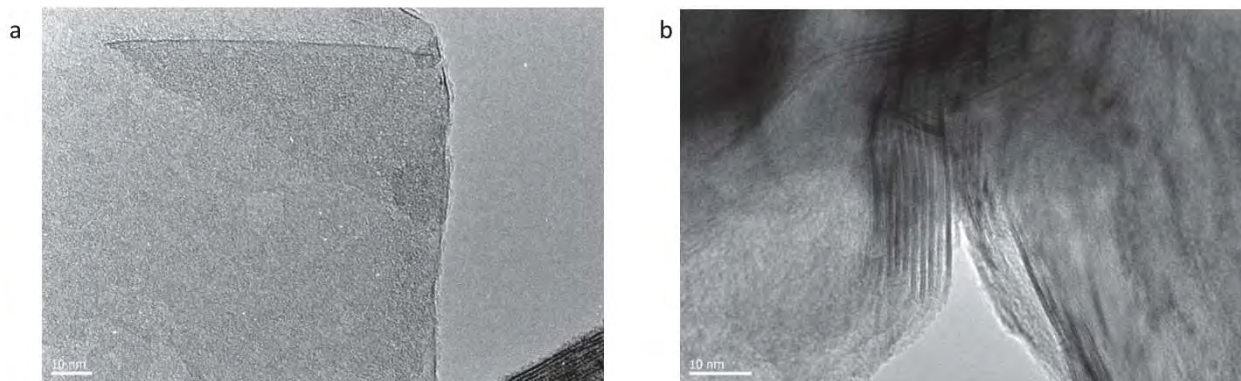

Supplementary Figure 5| TEM micrographs of hollow Ti₃C₂ spheres. **a,** edge of an individual $Ti_3C_2T_x$ flake, confirming presence of single-layer flakes and **b,** the connection point of two $Ti_3C_2T_x$ hollow spheres. They are with few layers and share some of them, indicating a good connection. This is important for the charge transfer throughout the entire macroporous framework.
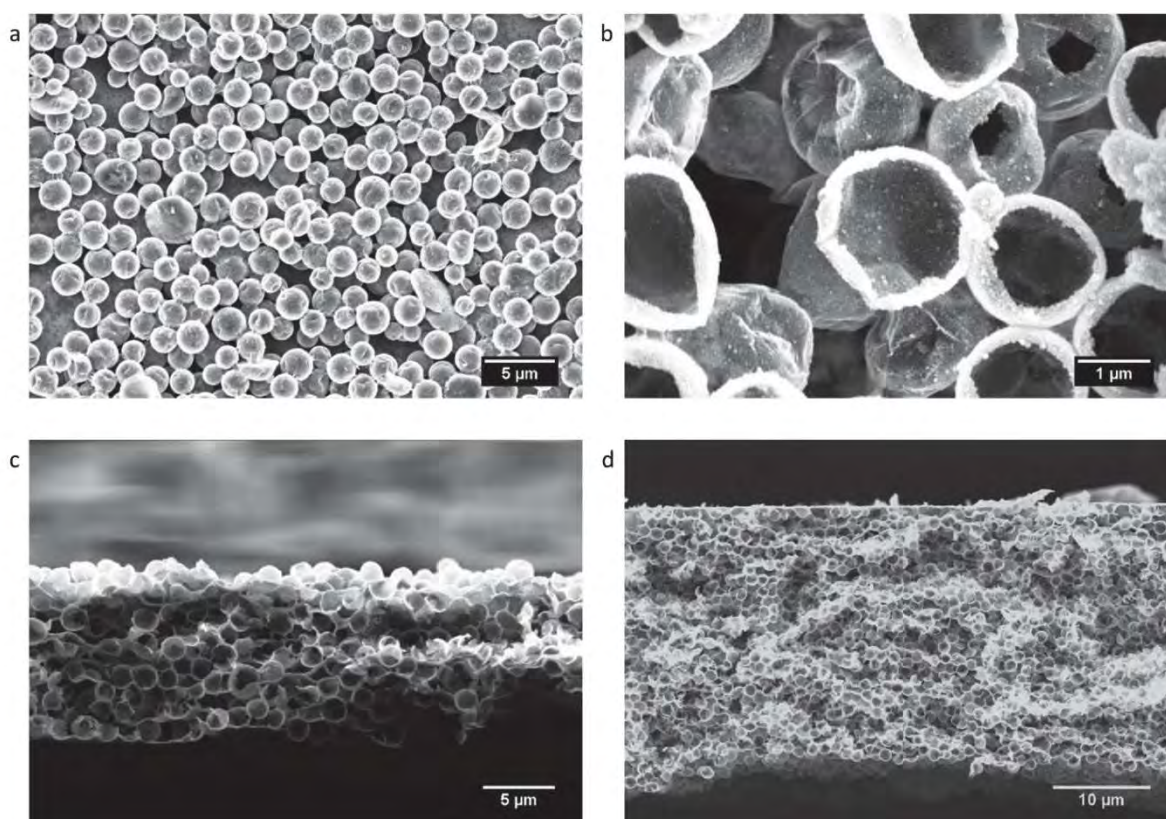
Supplementary Figure 6| Scanning electron micrographs of macroporous MXene films. **a,** few-layer $Ti_3C_2T_x$ wrapping PMMA spheres, **b,** $Ti_3C_2T_x$ wrapped PMMA after annealing in Ar at 400 °C, and **c,d,** cross-sections of $Ti_3C_2T_x$ and Mo_2CT_x films, respectively.
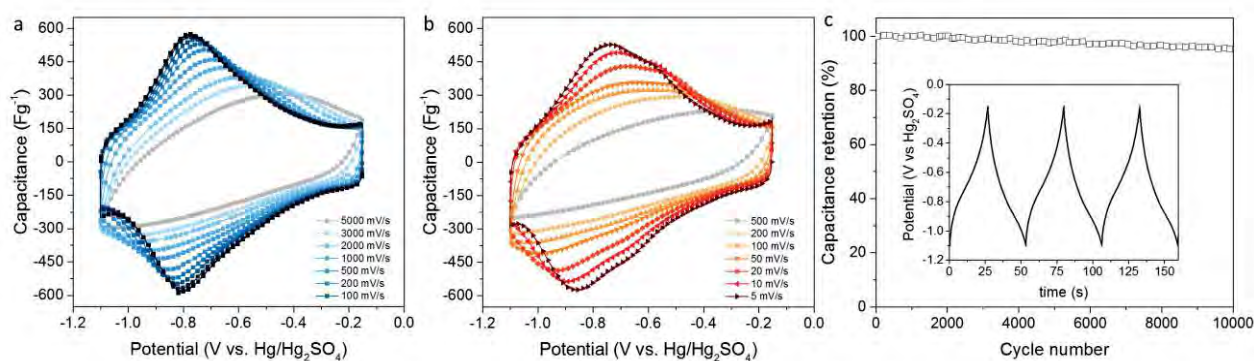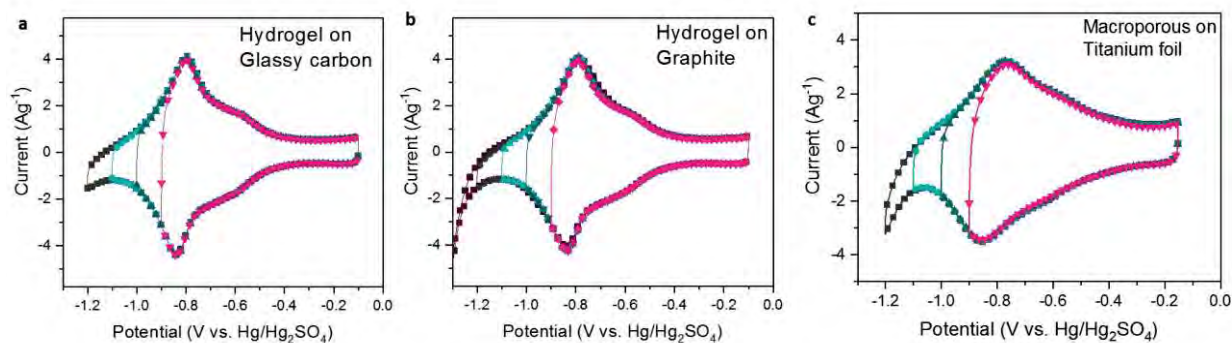

Supplementary Figure 7| a,b, Cyclic voltammetry profiles collected at different scan rates for macroporous $Ti_3C_2T_x$ films: **a,** 25 µm thick, loading of 0.9 mg/cm^2. **b**, 180 µm thick electrode, loading 4.3 mg/cm^2. **c,** Capacitance retention test of a 180 µm thick macroporous electrode performed by galvanostatic cycling at 10 A g^{-1}. Inset depicts galvanostatic cycling profiles collected at 10 A g^{-1}.
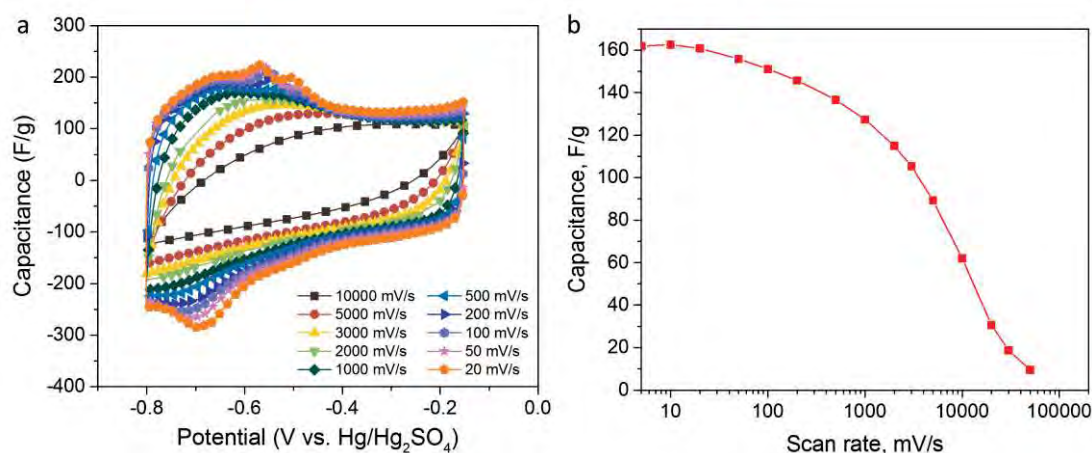
Supplementary Figure 8| Electrochemical performance of macroporous Mo₂CTₓ. a, Cyclic voltammetry profiles of a 30 µm thick macroporous Mo₂CTₓ film with 0.6 mg/cm² loading collected in 3 M H₂SO₄ at scan rates from 20 mV/s to 10000 mV/s, **b,** Rate performance of macroporous Mo₂CTₓ MXene film represented as mass-normalized capacitance.

Supplementary Figure 9| Electrochemical stability window for Ti₃C₂Tₓ electrodes collected at 5 mVs⁻¹ in 3 M H₂SO₄ with different current collectors. Cyclic voltammetry profiles for hydrogel Ti₃C₂Tₓ electrodes (2.65 mg/cm²) on **a,** glassy carbon and **b**, graphite current collector. **c**, Cyclic voltammetry profiles for macroporous Ti₃C₂Tₓ electrode (4.3 mg/cm²) on Ti foil.